33RD CONGRESS
OF THE INTERNATIONAL COUNCIL
OF THE AERONAUTICAL SCIENCES
STOCKHOLM, SWEDEN, 4-9 SEPTEMBER, 2022

ICAS 2022 SWEDEN

INVESTIGATION ON CRUISE PERFORMANCE OF A HAND-LAUNCHED SOLAR-POWERED UAV FOR ENVIRONMENTAL MONITORING IN TIBET

Kelei Wang[1], Zhou Zhou[1]

[1]College of Aeronautics, Northwestern Polytechnical University, Xi'an, China

Abstract

Aiming to realize long-endurance ecological environmental monitoring and rapid take-off and landing missions in Tibet, a hand-launched solar-powered unmanned aerial vehicle (HLSP UAV) in flying wing configuration is developed and introduced in this paper. Low-Reynolds-number (LRN) flow is quasi-steadily simulated by solving the full three-dimensional Reynolds Averaged Navier-Stokes (RANS) governing equations coupled with the k_T-k_L-ω transition model, while the propeller performance is evaluated using the multiple-rotating reference frame (MRF) method. The cruise performance of the present configuration is studied with and without consideration of the tractor propeller induced slipstream effects. The results indicate that the present configuration can satisfactorily meet the aerodynamic requirements of high-efficiency cruise missions, and the use of the new-concept high-performance propeller can improve the aerodynamic performance of the LRN aircraft to a certain extent.

Keywords: hand-launched solar-powered unmanned aerial vehicle; flying wing configuration; low Reynolds number; transition model; high-performance propeller.

1. Introduction

The abundant natural resources in Tibet play an important role in adjusting water resources and climate change in Asia and even in the world, however, as the human activities increased in recent years, non-negligible influences have been left on wild animals and plants in this region. Although various measures have been taken to reduce the impact on the ecological environment to the most extent, continuous monitoring is still necessary for identifying problems and making further improvements in a timely manner.

Due to the climate features[1] in Tibet, including low temperature, large difference in temperature between day and night, low atmospheric pressure and low oxygen content, it is neither feasible nor desirable to continuously monitor the ecological environments by manpower. Therefore, a continuous monitoring system based on a hand-launched solar-powered unmanned aerial vehicle (HLSP UAV) "MY-01" (see Fig.1) has been developed, which was adopted in the scientific investigations of Tibetan antelope in December 2018. In order to realize environment-friendliness and easy field assembling, a bionic configuration similar to a flying bird driven by two tractor propellers is used, and no rudder surface is equipped on this configuration except for an all-moving horizontal tail.

Figure 1 – The bionic hand-launched solar-powered UAV system MY-01.

In our above study, it was found that the MY-01 UAV had high cruise efficiency by using the large-aspect-ratio (LAS) low-Reynolds-number (LRN) wing, but it was difficult to achieve the required hand-launched takeoff targets in such a conventional configuration. Therefore, further improvements of MY-01 configuration have been carried out by our task group, as shown in Fig.2, a new HLSP UAV “MY-02” in flying wing configuration is developed.

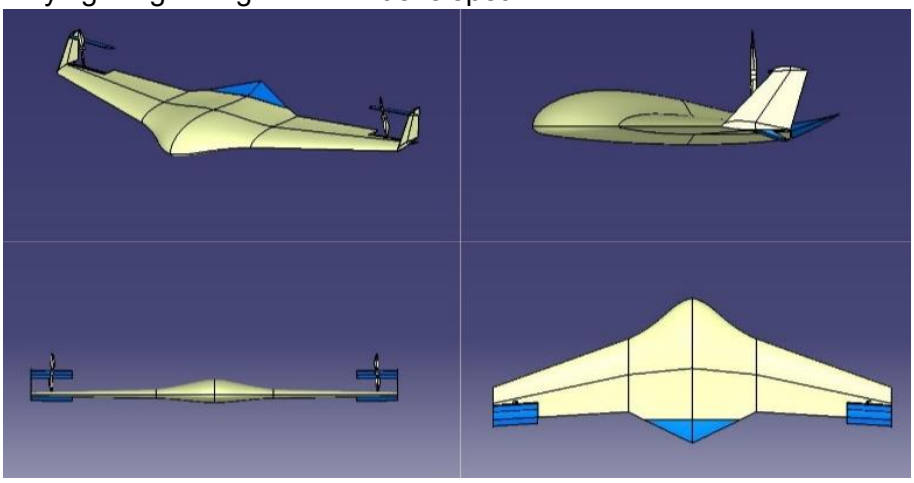

Figure 2 – Sketch of the hand-launched solar-powered UAV MY-02 (at takeoff).

The most significant change of MY-02 configuration with respect to the MY-01 configuration is the movement of the tractor propeller to the wing tip so as to form a special high lift device together with the wing surfaces. This helps to make good use of both the upper surface blowing (USB)[2] and the deflected slipstream[3] to generate enough lift at the low-speed hand-launched takeoff state, while the fuselage is only used to balance the pitching moment. Besides, it returns to the flying wing configuration at the cruise state to achieve excellent lift-to-drag performance. Although the main focus of the previous work is to improve the low-speed hand-launched takeoff performance, it is still the primary goal for the solar-powered UAV to perform long-endurance tasks with high cruise efficiency. Hence, this paper mainly studies the LRN aerodynamic performance of the MY-02 UAV at cruise.

On the other hand, it is well-known that the propeller has significant effects on the aerodynamic characteristics of the wing within slipstream at low-speed LRN states[4-8]. Analyses by Kroo[9], Veldhuis[10,11] and Kelei Wang et al.[12] indicated that significant aerodynamic benefits can be obtained through efficient utilization of the interactions between propeller and wing. Guided by the above results, the cruise performance and flow properties of the MY-02 UAV with and without the tractor propeller induced slipstream effects taken into account are numerically simulated and studied, furthermore, as shown in Fig.3, a new-concept high-performance propeller which is designed to deliver aerodynamic benefits for the wing within slipstream is also tested and compared with the traditional minimum induced loss (MIL) propeller at the specified thrust level. A detailed description of the high-performance propeller design process can be found in our previous work[13].

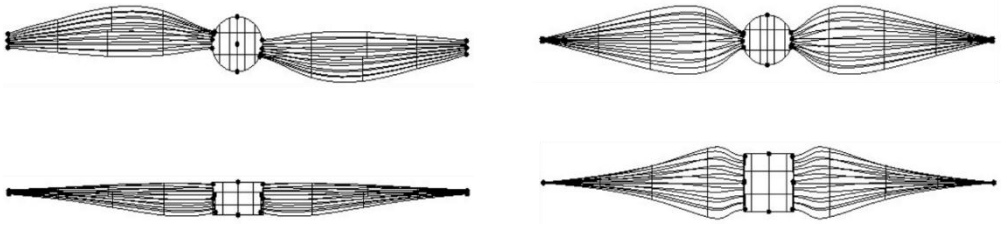

(a) Traditional MIL propeller (b) New-concept high-performance propeller

Figure 3 – Sketches of two types of propeller.

2. Numerical Methods

2.1 CFD Solver

In order to achieve accurate estimation of the boundary layer behaviors in modelling the complicated flow at LRN states, the full three-dimensional Reynolds Averaged Navier-Stokes (RANS) governing

are solved in the commercially available CFD package Fluent version 19.0. The RANS governing equations are discretized by the standard cell centered finite volume scheme. Air is considered as the ideal gas, and the LRN effects are considered by using the k_T-k_L-ω transition model[14,15] in which the modelled laminar kinetic energy (k_L) is used as the stream-wise non-turbulent fluctuations to predict the onset of transition. The second-order accurate Roe flux-difference upwind scheme is used for the convective fluxes of turbulence equations, and the lower-upper symmetric Gauss-Seidel (LU-SGS) implicit method is adopted for the time integration.

On the other hand, the multiple-rotating reference frame (MRF) method[16,17] is used to model the influences of propeller. The MRF method is a steady-state approximation that individual cell zones use different frame equations to solve RANS equations. Zones containing rotating components can then be solved using rotating reference frame equations, whereas stationary zones can be solved with stationary frame equations. At the interfaces between cell zones, a local reference frame transformation is performed to enable flow variables in one zone to be used to calculate fluxes at the boundary of the adjacent one. If rotating reference frame is used in a zone, the velocities and velocity gradients are converted from a rotating reference frame to the absolute inertial frame whereas the scalar quantities are determined locally from adjacent cells, because these vector quantities change with reference frame. In this way can greatly save the computational resources and also show

2.2 Multi-Block Hybrid Mesh

The computational mesh is generated by preprocessing codes ICEM for the three-dimensional model. Fig.4 shows the computational mesh around the half model of MY-02 configuration. The flow field is divided into three blocks for mesh generation: (1) the stationary region around the flying wing configuration with data-exchange interfaces associated with the rotational region, using unstructured mesh with prism layers, the non-dimensional distance for the first layer of cells away from the wall is set as $y^+ \approx 0.5$; (2) the rotational region around the propeller, using unstructured mesh; (3) the stationary region from the first block to the far field, using structured mesh.

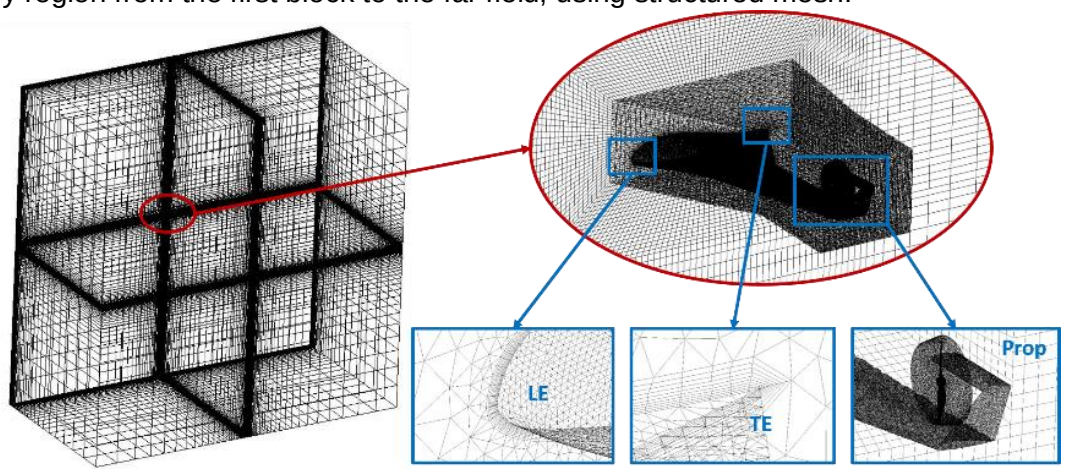

Figure 4 – Multi-block hybrid mesh around the half model of MY-02 configuration.

To examine the grid dependency in terms of results, a grid convergence study is conducted by using three levels of computational mesh with the same height of the first layer. Table 1 summarizes the total number of cells, computational time, and results corresponding to the three grid level.

Table 1 – Results of grid independence test for MY-02 configuration.

Grid	Number of cells	Computational time	C_L difference	C_D difference	C_M difference
Fine	1.3×10^7	13 h	/	/	/
Medium	9.3×10^6	7 h	0.55 %	1.47 %	0.93 %
Coarse	4.5×10^6	5 h	1.48 %	6.32 %	5.76 %

The difference in the lift, drag and pitching moment coefficients are found to be less than 1.5% for the results from the fine and medium grids, and less than 6.5% for the results from the fine and coarse grids, and the required computational time to get converged solutions starting from free-stream conditions for the medium and coarse grids are about 7 and 5 hours using the same work-

station with dual core, eight threads and 256G memory, therefore, the medium grid is selected for the following research.

2.3 Validations

To assess the accuracy and reliability of the present numerical methods in simulating the LRN flow around the MY-02 configuration with significant geometry features, the Eppler 387 airfoil[18,19], the biplane configuration with winglets[20], and the NACA 5868-9 propeller[21] are tested and validated against experimental data respectively.

2.3.1 Eppler 387 Airfoil

The Eppler 387 airfoil is extensively used in the numerical validation of two-dimensional (2-D) LRN flow. In the current study, an unstructured mesh is created with prism layers to improve mesh quality. Besides, the non-dimensional y-plus of the near-wall grids is set to be about 0.1 in the direction normal to the wall. Fig.5 illustrates the computational mesh around the Eppler 387 airfoil. A full-state type boundary condition is imposed at the far field of the computational domain, and a non-slip adiabatic boundary condition is used on the surface of the airfoil.

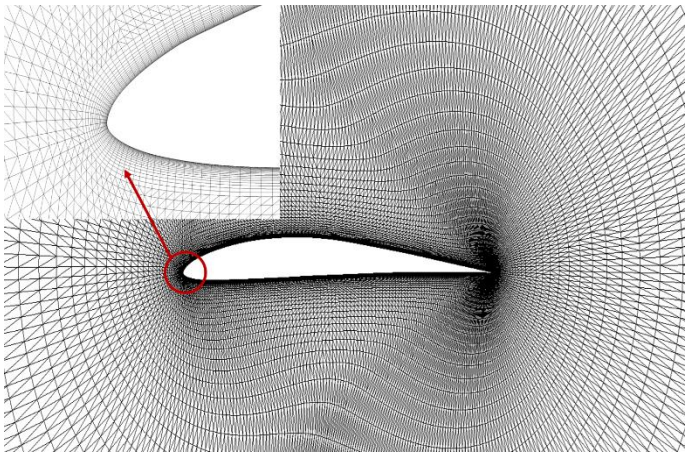

Figure 5 – Computational mesh around the Eppler 387 airfoil.

The aerodynamic results of the Eppler 387 airfoil based on the k_T-k_L-ω transition model for Re_c=1.0×10^5 and Re_c=3.0×10^5 (see Fig.6) are compared with data taken from the Low-Turbulence Pressure Tunnel of NASA Langley Research Center. As seen, all the computational results are in good agreement with the experimental data for both the calculated values and the predicted trends. Fig.7 depicts the comparison of the pressure distribution for angle of attack (AOA) values of α=0° and α=2° at the low Reynolds number of Re_c=1.0×10^5. It indicates that the k_T-k_L-ω transition model is capable of accurately predicting the formation of laminar separation bubble (LSB) on the upper surface of airfoil.

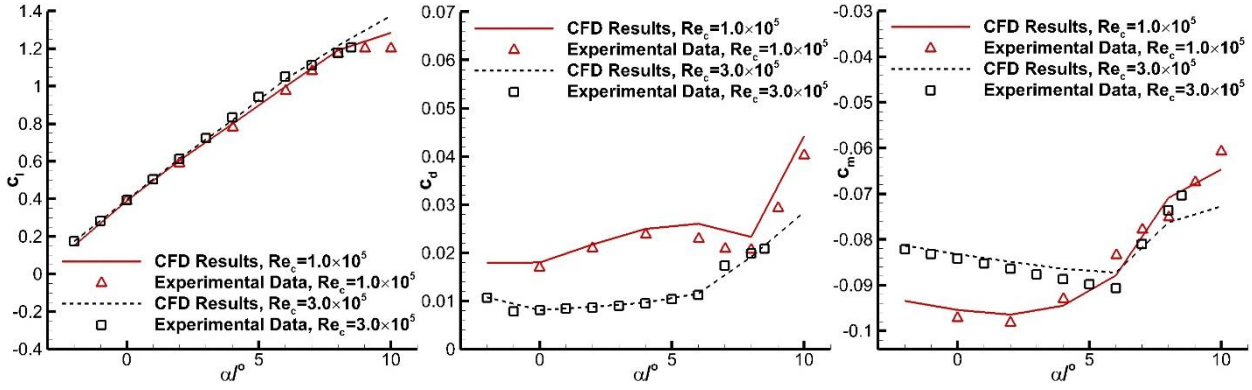

(a) c_l-α (b) c_d-α (c) c_m-α

Figure 6 – Comparison of aerodynamic force coefficients generated by the Eppler 387 airfoil.

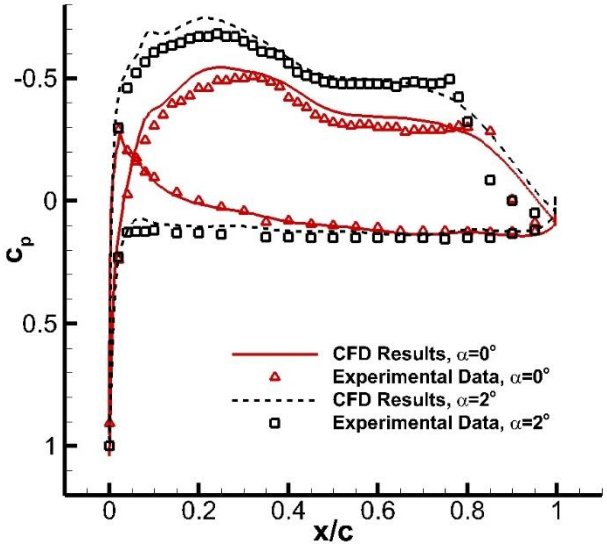

Figure 7 – Comparison of pressure distribution around the Eppler 387 airfoil at Re_c=1.0×10^5.

2.3.2 Biplane Configuration with Winglets

The C-shaped wingtip plays an important role in determining the aerodynamic performance of the MY-02 configuration. Therefore, a typical biplane configuration with winglets (see Fig.8) with a decalage angle of 0° at Re_c=5.1×10^5 is numerically studied. The aerodynamic results are compared with data taken from the Pennsylvania State University subsonic wind tunnel in Fig.9, the experimental accuracies are determined: C_D±0.0005, C_L±0.02, and α±1°. It can be seen that the overall agreement with experimental data at all angles of attack is satisfactory, and only a slight discrepancy of the drag coefficient exists when $\alpha \geqslant 8°$.

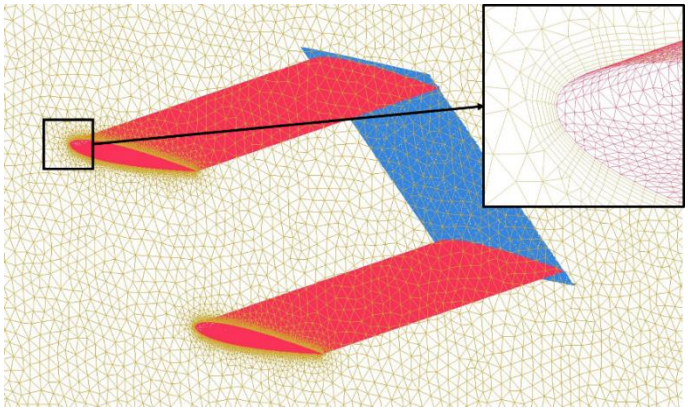

Figure 8 – Computational mesh around the biplane configuration with winglets.

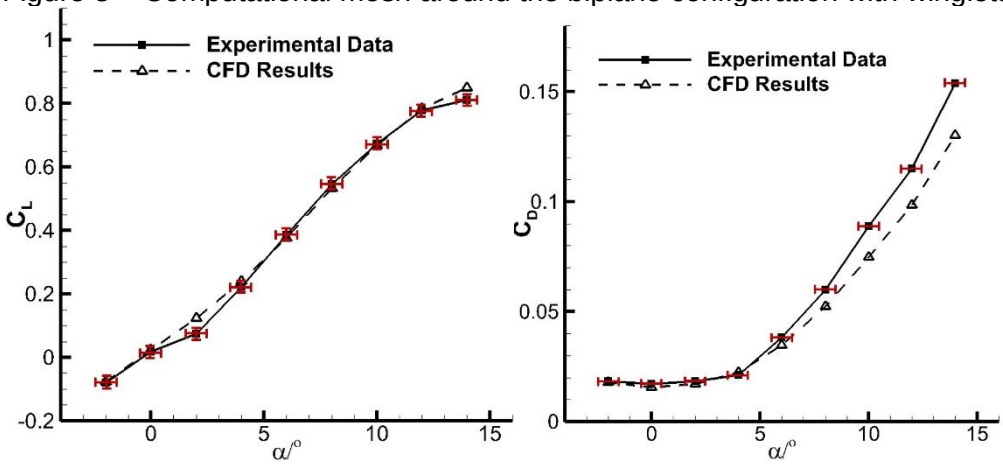

(a) C_L-α (b) C_D-α

Figure 9 – Comparison of aerodynamic force coefficients generated by the biplane configuration with winglets.

2.3.3 NACA 5868-9 Propeller

The NACA 5868-9 propeller is a typical two-blade propeller with Clark Y sections, its three-dimensional (3-D) computational mesh are depicted in Fig.10, and the detailed operating condition are illustrated in Table 2. The numerical results are compared with data taken from the NACA 20-foot wind tunnel in Fig.11. It can be seen that the numerical results are in close agreements with the experimental data for both the calculated values and the predicted trends, and the maximum relative error is less than 10% at all these advanced ratios.

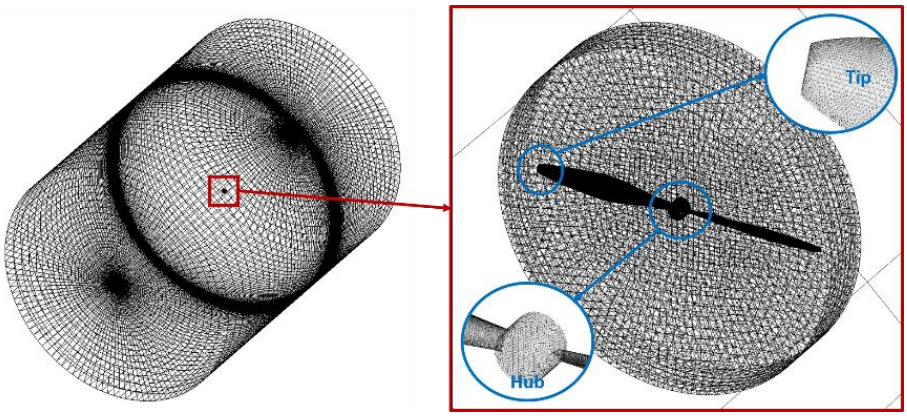

Figure 10 –Computational mesh around the NACA 5868-9 propeller.

Table 2 – Operating condition of NACA 5868-9 propeller case.

Parameter	Value
Diameter	3.048 m
Collective pitch	25°
Free-stream velocity	50.4 m/s
Ambient pressure	96611.4 Pa
Ambient temperature	285.55 K
Ambient density	1.17865 kg/m^3
Altitude	400 m

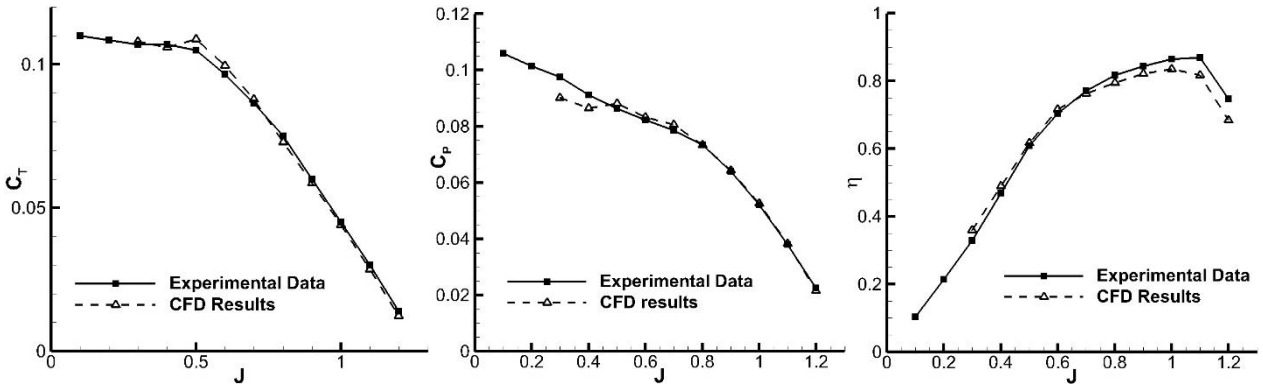

(a) C_T-J (b) C_P-J (c) η-J

Figure 11 – Comparison of propulsive properties of the NACA 5868-9 propeller.

3. Cruise Performance Analysis

Table 3 lists the cruise state parameters of the MY-02 HLSP UAV.

Table 3 – Cruise state parameters of the MY-02 hand-launched solar-powered UAV.

Parameter	Value	Parameter	Value
Total mass	3 kg	Cruise speed	15.0 m/s
Altitude	6000 m	Chord Reynolds number	2.48×10^5
Wing area	1.0 m^2	Cruise lift coefficient	0.4
Span	2.5 m	Propeller type	APC 1070
Chord length	0.4 m	Propeller rotational speed	5000 rpm

3.1 Aerodynamic Force Variations

Fig.12 depicts the cruise performance of the flying wing configuration at the cruise state from α=-6° to α=20°, both propeller-off and propeller-on states are considered. At the propeller-off state, the linearity of both the lift curve and the pitching moment curve is quite good within the AOA range from α=-6° to α=14°, a pitching static margin of near 7.5% is obtained, and the lift-to-drag ratio (C_L/C_D) reaches 19.0 at C_L=0.4, which meets the cruise requirements very well. However, when the propeller induced slipstream effects are considered, both the lift curve slope and the maximum lift coefficient are reduced, the drag are increased slightly at the same time, which leads to a maximum lift-to-drag ratio reduction of approximately 14.6%. Besides, the stall occurs earlier, and the pitching moments generated by the flying wing configuration after stall are significantly decreased at the propeller-on state when compared to that at the propeller-off state.

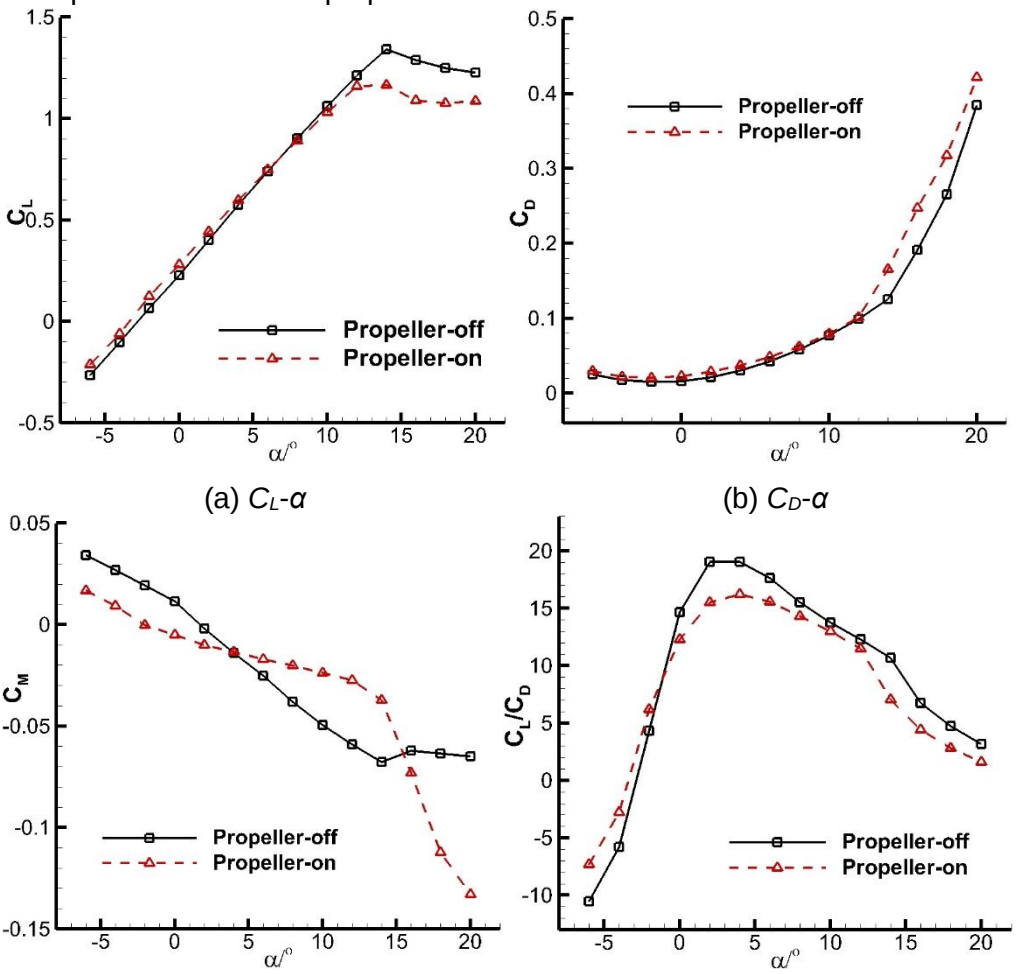

(a) C_L-α (b) C_D-α

(c) C_M-α (d) C_L/C_D-α

Figure 12 – Cruise performance of the flying wing configuration at both propeller-off and propeller-on states.

3.2 Low Reynolds Number Flow Properties Comparison

Fig.13 and Fig.14 depicts the flow developments of the flying wing configuration from α=0° to α=12° at both propeller-off and propeller-on states, the distributions of both turbulent viscosity ratio (μt) and near-wall stream-lines are visualized on the upper surfaces of the main wing and the above wing. In Fig.14, a “box” is used to represent the area affected by the propeller induced slipstream, both the up-wash side (UWS) and down-wash side (DWS) are marked according to the propeller rotational direction. It should be noted that the present numerical method can only be used for qualitative analyses of the flow developments, but cannot quantitatively describe the flow characteristics because it is obviously unsteady.

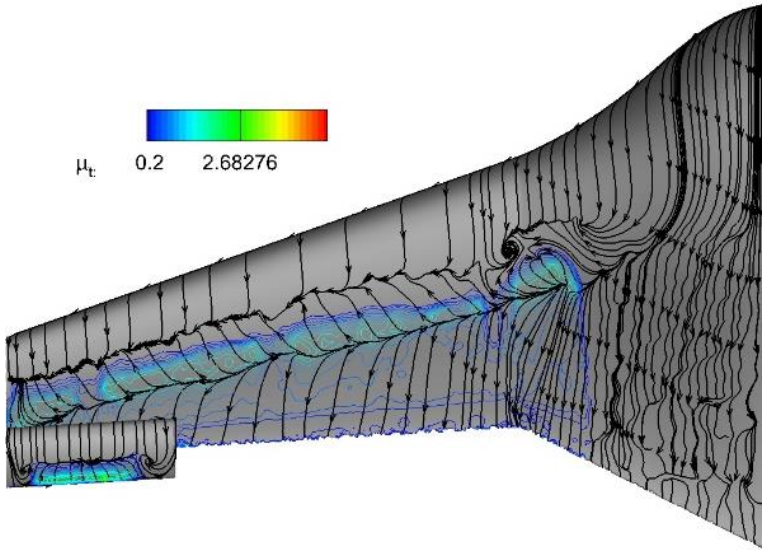

(a) α=0°

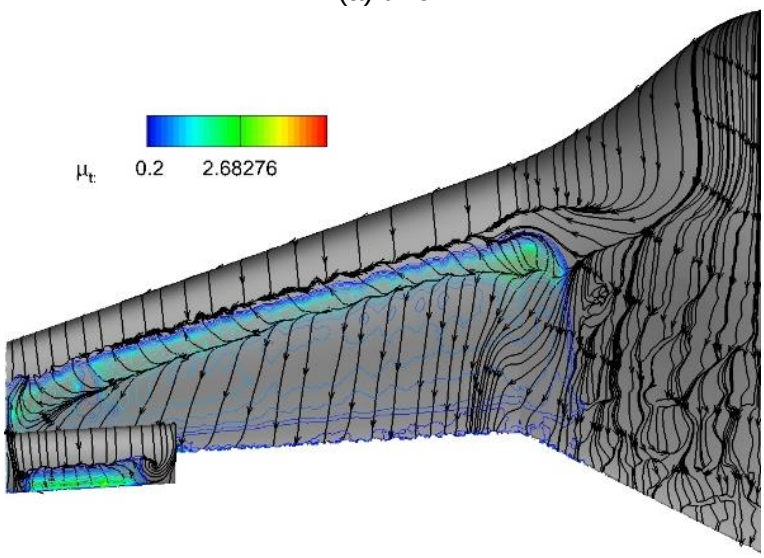

(b) α=4°

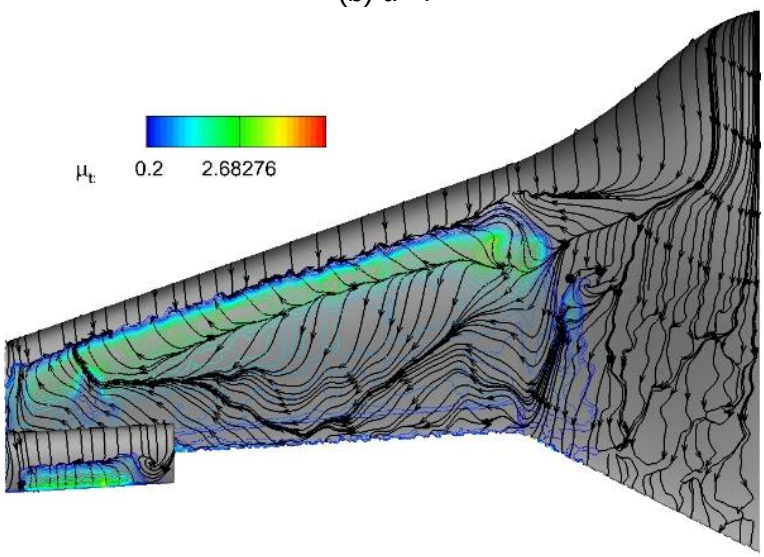

(c) α=8°

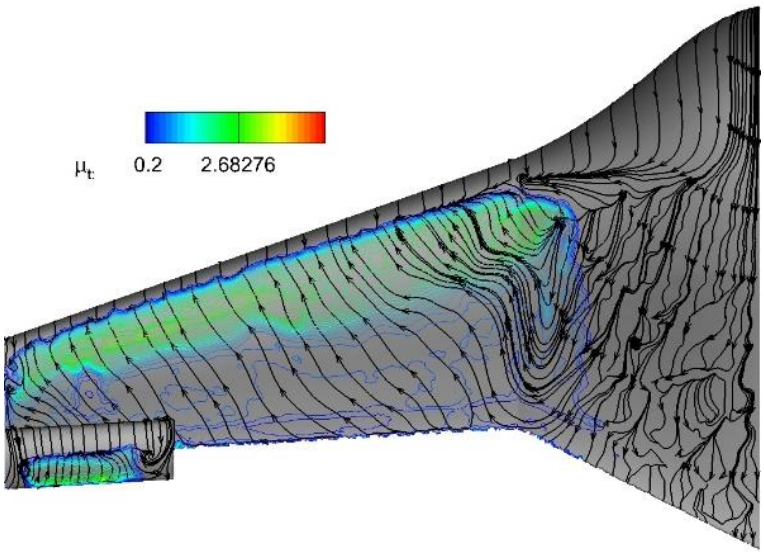

(d) α=12°

Figure 13 – Flow properties distributed on the upper surface of the flying wing configuration at the propeller-off state.

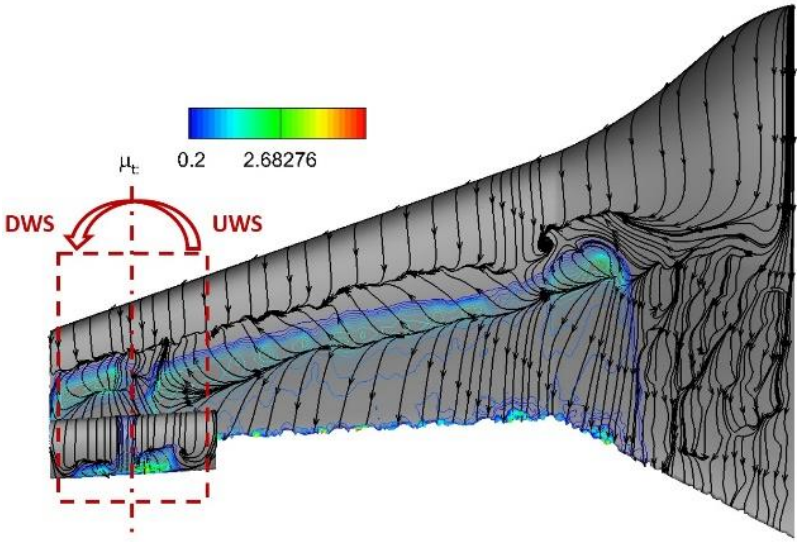

(a) α=0°

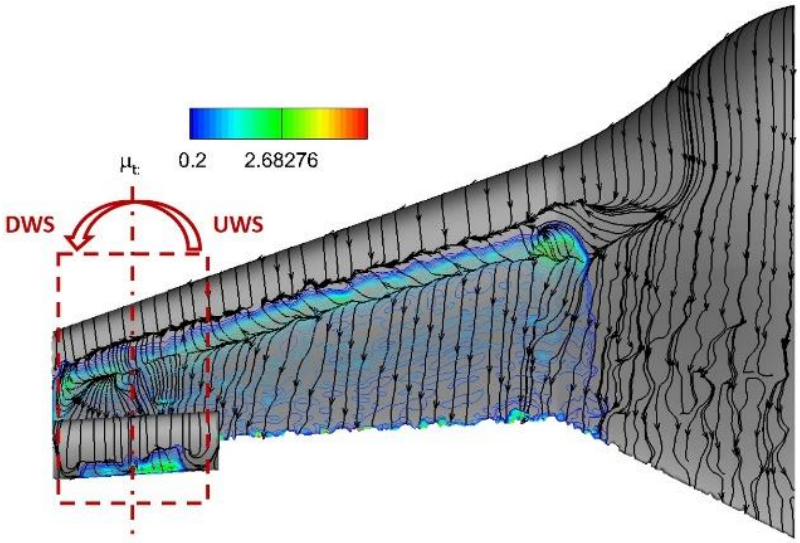

(b) α=4°

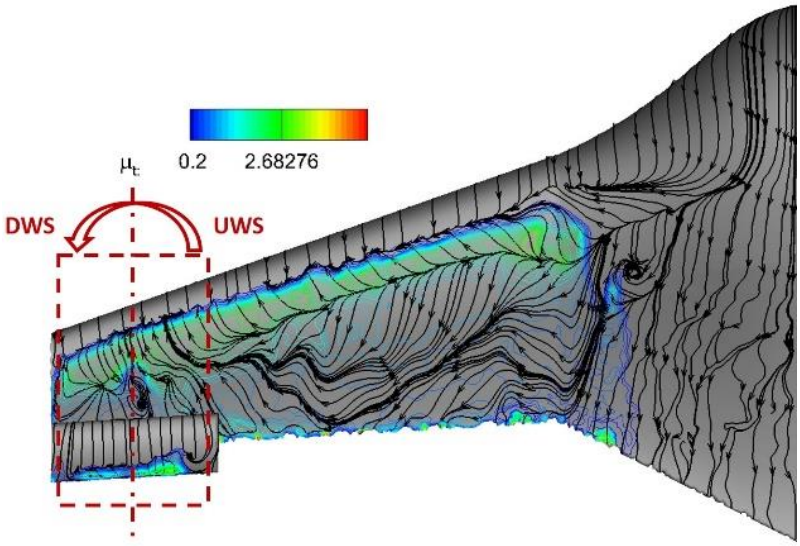

(c) α=8°

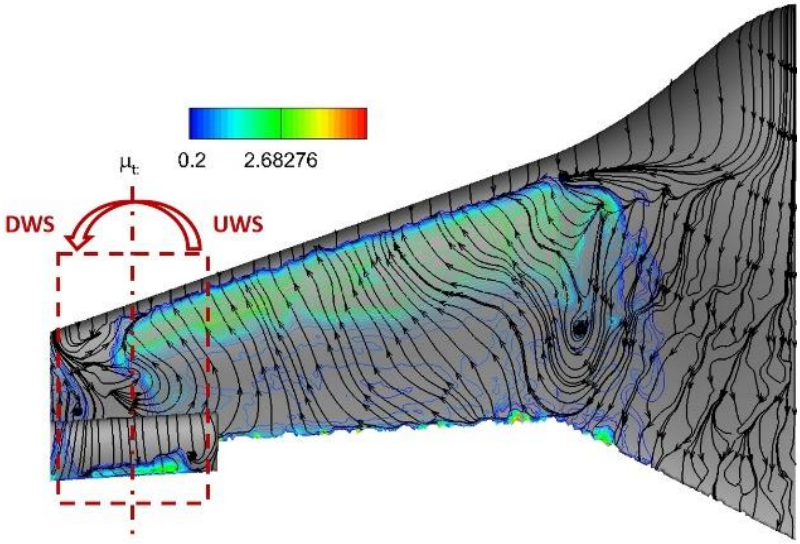

(d) α=12°

Figure 14 – Flow properties distributed on the upper surface of the flying wing configuration at the propeller-on state.

For the flying wing configuration at the propeller-off state, it can be found that: (1) the typical LSB structure is formed on the upper surface of the main wing at small AOAs, and as the AOA increased, the LSB moves forward and its length is decreased gradually, however, laminar separation and flow transition occur on the above wing but the separated flow does not reattach to the wing surface at all these AOAs; (2) due to the existence of the C-shaped wingtip, no obvious wingtip vortices can be found on the main wing, but on the above wing, a clear transverse separated vortex structure can be seen under the interaction between the wingtip vortex and the laminar separated flow; (3) the enhancement of the span-wise flow on the main wing causes the separated flow to no longer reattach to the wing surface after laminar separation, this occurs locally near the wingtip at α=8°, but complete separated flow after laminar separation is formed on the outer section of the main wing at α=12°.

When the propeller induced slipstream effects are considered, the overall development trends of the flow-field around the flying wing configuration has not been changed significantly at such a low thrust level to cruise except for the near-wall flow within the propeller action region. In details, the propeller induced rotating flow makes the main wing on the windward side and the leeward side operating in different LRN regimes: (1) the flow transition on the windward side is advanced at small AOAs due to the energy injection from the propeller induced rotating flow, while the flow transition on the leeward side is delayed. This causes the length of the LSB on both sides obviously different from each other (see Fig.14 (a) and (b)); (2) the perturbation induced by the propeller rotational motion makes the separated flow on the main wing at high AOAs so complicated that it is difficult to find

effective mechanisms to describe, this is mainly due to the flow hedging between the propeller induced rotating flow and the span-wise flow inherently generated by the present flying wing configuration. On the other hand, the near-wall flow properties distributed on the above wing have also undergone extremely significant changes: (1) the local AOA of the above wing within the propeller induced slipstream does not change significantly as the AOA of the incoming flow changed, which further makes the locations of both laminar separation and flow transition on the upper surface of the above wing almost unchanged at all these AOAs. This ensures that the lift generated by the above wing can be maintained at a relatively large value even when the flying wing configuration has stalled, thereby avoiding the reversal of pitching moment trend at high AOAs (see Fig.12(c)); (2) both the laminar separation location and the flow transition location on the UWS are more forward than that on the DWS, this is because of the propeller rotational effects; (3) a localized region in the middle of the above wing transits from the LE at α=0° due to the propeller acceleration effects, the flow within this region is completely attached while notable transverse vortex structures are formed on both sides of this region. Furthermore, the above phenomenon gradually disappears as the AOA increased, this may be related to the specified low thrust level at cruise.

4. High-Performance Propeller Induced Improvements

With the rapid development of distributed electric propulsion (DEP) vehicles in recent years, Patterson et al.[22,23] and Wang et al.[13,24] proposed new concepts of high-lift or high-performance propeller, which aim to improve the global aerodynamic performance of the whole aircraft. Therefore, we designed a high-performance propeller with the same diameter, sectional airfoil geometry and specified thrust constraints, and used it to replace the traditional MIL propeller for numerical analysis (see Fig.3). Table 4 lists the detailed aerodynamic force coefficients generated by the flying wing configuration under different propeller induced slipstream effects.

Table 4 – Comparison of the aerodynamic performance of the flying wing configuration under different propeller induced slipstream effects.

Propeller type	α(°)	$C_{L(1)}$	C_D	C_M	C_L/C_D	T(N)	Q(Nm)	η
MIL (n=5000rpm)	0	0.2815	0.02291	-0.00513	12.286	0.88123	0.04053	0.6230
	4	0.5965	0.03679	-0.01331	16.212	0.84687	0.03990	0.6080
	8	0.8917	0.06224	-0.01710	14.327	0.83317	0.03984	0.5991
	12	1.1591	0.10099	-0.02731	11.477	0.82877	0.04006	0.5927
	16	1.0884	0.24713	-0.07301	4.404	0.85065	0.04159	0.5859
High-Performance (n=4650rpm)	0	0.2855	0.02301	-0.00518	12.408	0.86286	0.04114	0.6530
	4	0.614 1	0.03696	-0.01347	16.616	0.83616	0.04044	0.6438
	8	0.9194	0.06295	-0.02358	14.606	0.81712	0.03981	0.6392
	12	1.1964	0.10232	-0.03161	11.692	0.81462	0.03962	0.6402
	16	1.1157	0.24849	-0.07673	4.490	0.82162	0.04002	0.6393

It can be seen that the lift, the drag, the nose-down pitching moment and the lift-to-drag ratio generated by the flying wing configuration at all these AOAs under the described high-performance propeller induced effects are slightly increased when compared with the traditional MIL propeller induced results, besides, the propulsive efficiencies of the high-performance propeller are higher than that of the traditional MIL propeller at all these AOAs. This means that, the new-concept high-performance propeller is especially suitable for propeller-driven aircrafts, because it can effectively improve the aerodynamic efficiency of the wing and the propulsive efficiency at the same time, which shows great advantages energy utilization.

As shown in Fig. 15, totally 6 cross sections in the stream-wise direction are selected to conduct analyses on the development of flow properties, the x-coordinate of each cross section in the stream-wise direction is respectively: x =0.58 m, x = 0.6 m, x = 0.62 m, x = 0.64 m, x = 0.66 m, x = 0.68 m. Fig. 16 and Fig. 17 compare the axial velocity distributions on the cross sections under the effects induced by these two types of propeller. As compared with the traditional MIL propeller induced results, the significant changes of the high-performance propeller in the distributions of both chord length and twist angle cause that the radial position of the maximum induced axial velocity slightly moves towards the propeller hub, so that a larger range of the above wing are in the high-speed flow

regime with higher dynamic pressure, which results in larger aerodynamic forces, including lift, drag and nose-down pitching moment. Besides, the smaller and weaker propeller tip vortex caused by the significant reduction of wing tip chord length of the high-performance propeller may be the main reason for the increase of propeller propulsive efficiency, which is not the focus of this paper and needs further research and proof.

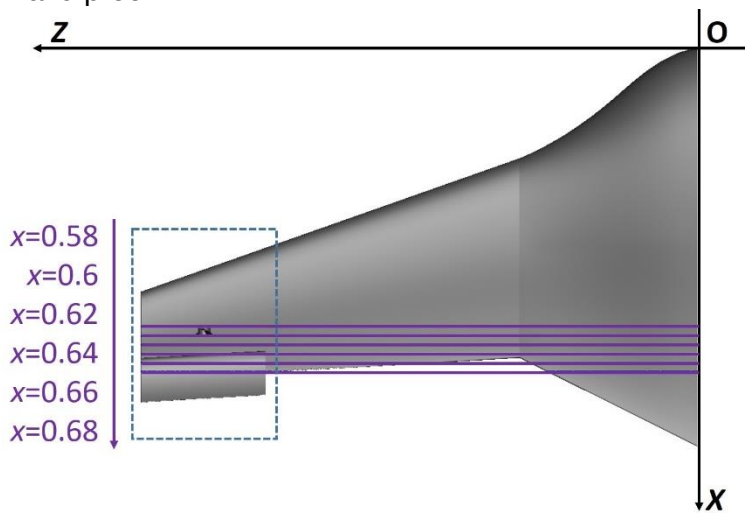

Figure 15 – Cross sections in front of and behind the tractor propeller in stream-wise direction.

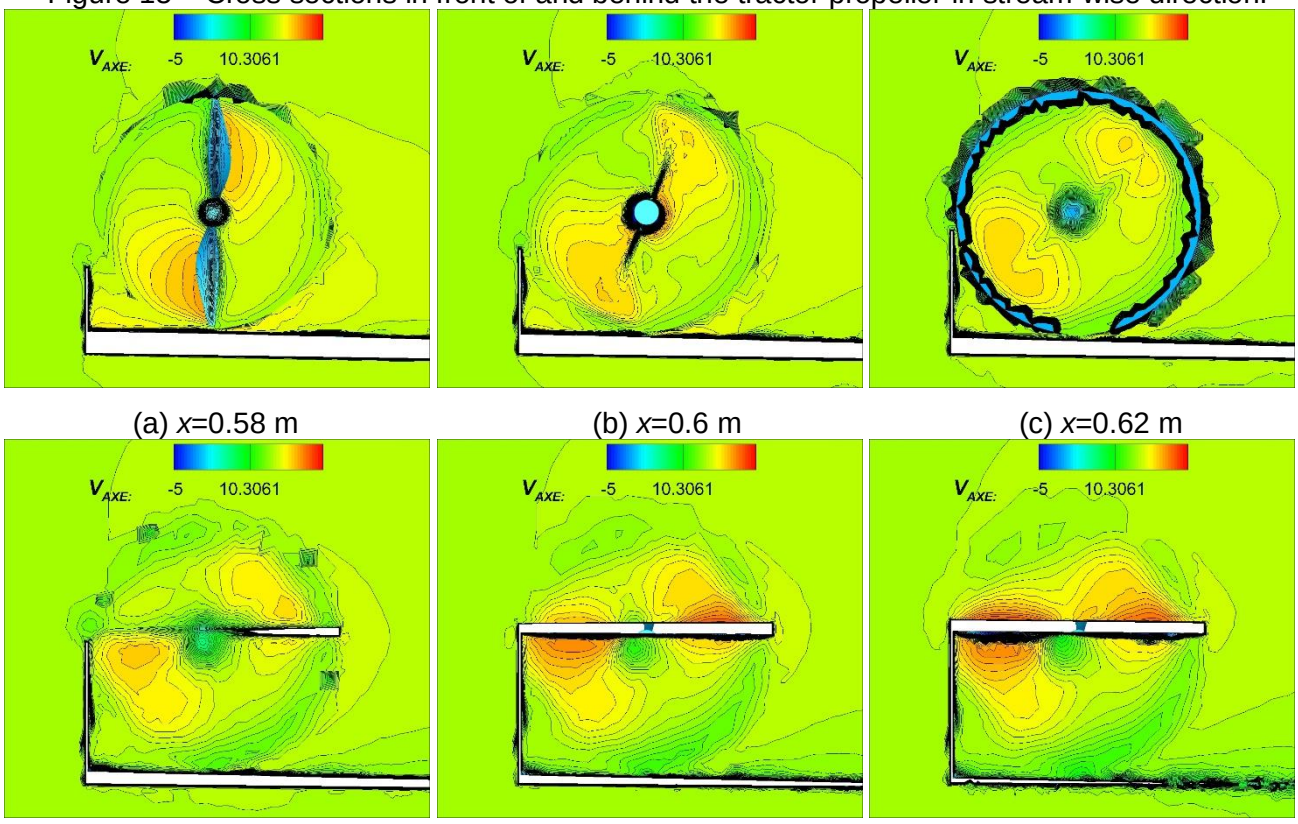

(a) *x*=0.58 m (b) *x*=0.6 m (c) *x*=0.62 m

(d) *x*=0.64 m (e) *x*=0.66 m (f) *x*=0.68 m

Figure 16 – Axial velocity distributions at different cross sections under the traditional MIL propeller induced effects.

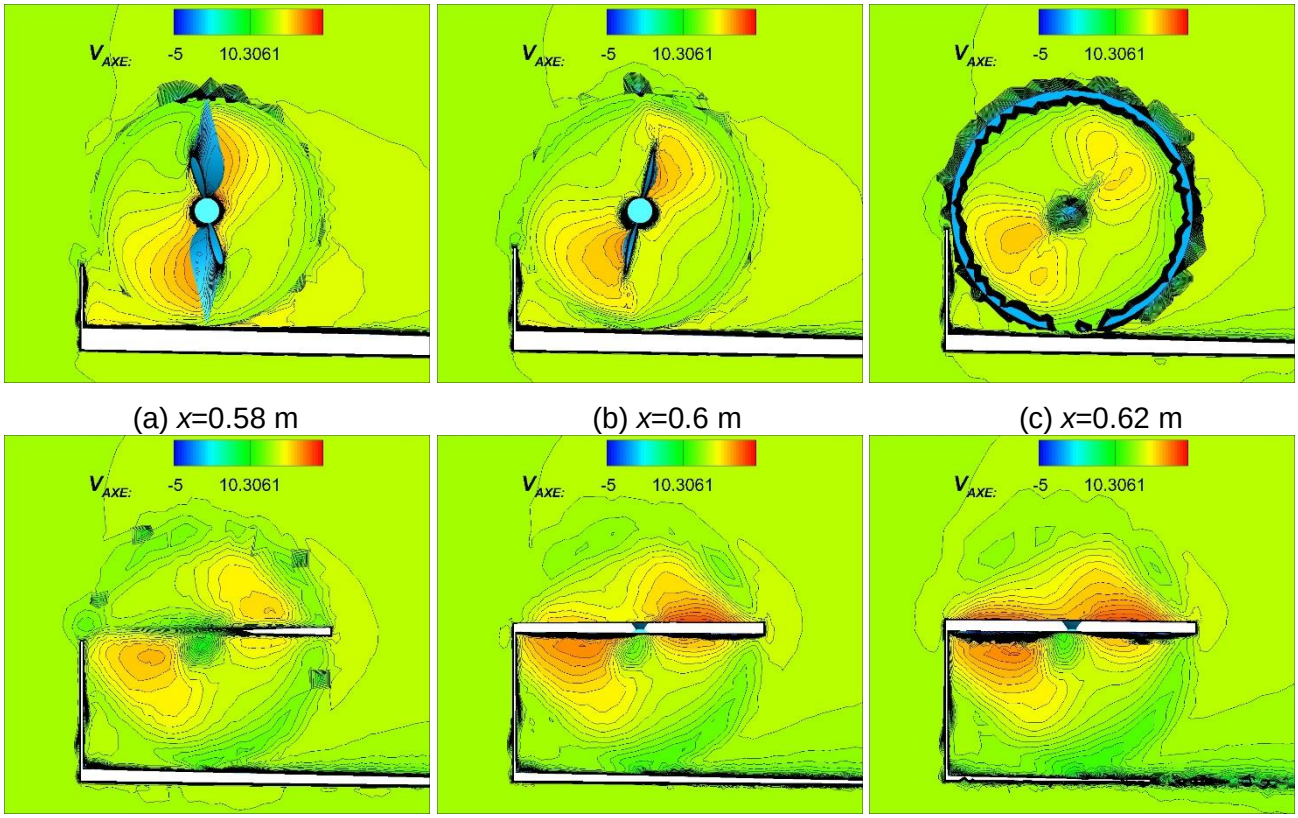

(a) x=0.58 m (b) x=0.6 m (c) x=0.62 m

(d) x=0.64 m (e) x=0.66 m (f) x=0.68 m

Figure 17 – Axial velocity distributions at different cross sections under the high-performance propeller induced effects.

5. Conclusion

To meet the increasing needs for long-endurance aerial ecological environmental monitoring in Tibet, a hand-launched solar-powered UAV in flying wing configuration is introduced and studied in this paper. The ability of the numerical methods to accurately compute the LRN transitional flows is evaluated via experimental case validations. The numerical analysis results based on the k_T-k_L-ω transition model and the MRF technique show good agreement with the experimental results. Then, the cruise aerodynamic analysis is performed in detail. The results indicate that:

(1) A maximum lift-to-drag ratio (CL/CD) of 19.0 and pitching moment self-balancing (CM≈0.0) at CL=0.4 can be obtained at the same time by the MY-02 hand-launched solar-powered UAV at propeller-off state, which meets the cruise requirements very well. However, when the propeller induced slipstream effects are considered, the lift-to-drag performance becomes worse with a maximum lift-to-drag ratio reduction of approximately 14.6%, but the pitching stability at high AOAs is improved from static instability to static stability.

(2) At propeller-off state, the typical LSB structure formed on the upper surface of the main wing plays significant role in determining the aerodynamic performance of the flying wing configuration, and the enhancement of the span-wise flow at high AOAs will lead to totally flow separation on the outer section of the main wing, which is the main cause of stall. Besides, the existence of the C-shaped wingtip can effectively reduce the intensity and scale of wingtip vortex, and only the transverse separated flow caused by the interaction between the wingtip vortex and the laminar separated flow exists on the upper surface of the above wing.

(3) At propeller-on state, the low Reynolds number flow properties of the flying wing configuration has not been changed significantly at such a low thrust level except for the near-wall flow within the propeller action region. For the main wing, the flow transition is advanced on the windward side but delayed on the leeward side at small AOAs, besides, the near-wall flow is so complicated under the tractor propeller at high AOAs that it is difficult to find effective mechanisms to describe, which is mainly due to the flow hedging between the propeller induced rotating flow and the span-wise flow inherently generated by the flying wing configuration. For the above wing, the local AOA within the

propeller slipstream does not change significantly, which ensures that the lift generated by the above wing can be maintained at a relatively large value even when the flying wing configuration has stalled, thereby avoiding the reversal of pitching moment trend at high AOAs, besides, both the laminar separation location and the flow transition location on the UWS are more forward than that on the DWS, and significant transverse vortex structures are formed on both sides of the slipstream region. (4) The use of the new-concept high-performance propeller can improve the aerodynamic efficiency and the propulsive efficiency of the flying wing configuration at low Reynolds numbers to a certain extent, and shows great advantages energy utilization. This is mainly related to the variation of induced axial velocity distributions within slipstream, and needs further research and proof in our future research.

6. Contact Author Email Address

Mailto: craig-wang@nwpu.edu.cn

7. Copyright Statement

References

[1] X. Li, Y. Fu and X. Hu. Kinetics study of SBR process on Qinghai & Tibet plateau. Industrial safety and environmental protection, Vol. 30, pp 15-16, 2004.

[2] T. Xiao, Z. Zhu, S. Deng, et al. Effects of nozzle geometry and active blowing on lift enhancement for upper surface blowing configuration. Aerospace Science and Technology, Vol. 111, pp 106536, 2021.

[3] G. Cui, L. Feng and W. Wang. Aerodynamic characteristic of deflected slipstream aimed at vertical takeoff and landing. Journal of Aircraft, Vol. 56, No. 4, pp 1418–1426, 2019.

[4] A. Ehab, P. Colin. Experimental investigation of the effect of propeller slipstream on boundary layer behavior at low Reynolds number. AIAA Paper 2000-4123, 2000.

[5] F. Catalano. On the effect of an isolated propeller slipstream on wing aerodynamic characteristics. Acta Polytechnica. Vol. 44, No. 3, pp 8–14, 2004.

[6] S. Miley, R. Howard and B. Holmes. Wing laminar boundary layer in the presence of a propeller slipstream. Journal of Aircraft, Vol. 25, No. 7, pp 606–611, 1988.

[7] F. Makino, H. Nagai. Propeller slipstream interference with wing aerodynamic characteristics of Mars airplane at low Reynolds number. *52nd Aerospace Sciences Meeting*, pp. 1-12, 2014.

[8] K. Wang, X. Zhu, Z. Zhou, H. Wang. Distributed electric propulsion slipstream aerodynamic effects at low Reynolds number. Acta Aeronautica et Astronautica Sinica, Vol. 37, No. 9, pp 2669–2678, 2016.

[9] I. Kroo. Propeller-wing integration for minimum induced loss. Journal of Aircraft, Vol. 23, No. 7, pp 561-562, 1986.

[10] L. Veldhuis. Optimization of tractor propeller-wing configurations. Journal of Elections Public Opinion & Parties, Vol. 209, No. 37, pp 215–226, 1995.

[11] L. Veldhuis. Aerodynamic optimization of wings in multi-engined tractor propeller arrangements. Aircraft Design, Vol. 3, No. 3, pp 129–149, 2000.

[12] K. Wang, Z. Zhou, X. Zhu, X. Xu. Aerodynamic design of multi-propeller/wing integration at low Reynolds numbers. Aerospace Science and Technology, Vol. 105, pp 105991, 2020.

[13] K. Wang, Z. Zhou, Z. Fan, J. Guo. Aerodynamic design of tractor propeller for high-performance distributed electric propulsion aircraft. Chinese Journal of Aeronautics, Vol. 34, No. 10, pp 20-35, 2021.

[14] J. Morgado, R. Vizinho, M. Silvestre, J. Pascoa. XFOIL vs CFD performance predictions for high lift low Reynolds number airfoils. Aerospace Science and Technology, Vol. 52, pp 207–214, 2016.

[15] R. Volino. A new model for free-stream turbulence effects on boundary layers. Journal of Turbomachinery, Vol. 120, pp 613-620, 1998.

[16] Z. Liu, R. Albertani, J. Moschetta, et al. Experimental and computational evaluation of small micro coaxial rotor in hover. Journal of Aircraft, Vol. 48, No. 1, pp 220–229, 2011.

[17] T. Zhang, G. Barakos. High-fidelity numerical analysis and optimisation of ducted propeller aerodynamics and acoustics. Aerospace Science and Technology, Vol. 113, pp 106708, 2021.

[18] M. Selig, J. Guglielmo. High-lift low Reynolds number airfoil design. Journal of Aircraft, Vol. 34, pp72–79, 1997.

[19] G. Cole, T. Mueller. Experimental measurements of the laminar separation bubble on an Eppler 387 airfoil at low Reynolds numbers. https://ntrs.nasa.gov/search.jsp?R=19900006064 2019-10-21T09:54:51+00:00Z, UNDAS-1419-FR, 1990.

[20] P. D. Gall, H. C. Smith. Aerodynamic characteristics of biplanes with winglets. Journal of Aircraft, Vol. 24, No. 8, pp 518-522, 1987.

[21] E. Hartman, D. Biermann. The aerodynamic characteristics of full-scale propellers having 2, 3, and 4 blades of Clark y and R.A.F. 6 airfoil sections. TR-640, the United States: National Advisory Committee for Aeronautics, 1938.

[22] M. Patterson, J. Derlaga, N. Borer. High-lift propeller system configuration selection for NASA's SCEPTOR distributed electric propulsion flight demonstrator. *16th AIAA aviation technology, integration, and operations conference*, 2016.

[23] M. Patterson. *Conceptual design of high-lift propeller systems for small electric aircraft*. Georgia Institute of Technology, 2016.

[24] K. Wang, Z. Zhou, X. Zhu, et al. Reconstruction design of propeller induced flow-field based on aerodynamic loading distributions. Acta Aeronautica et Astronautica Sinica, Vol. 41, No. 1, pp 123118, 2020.